Proton Radiography for a Small-Animal Irradiation Platform Based on a Miniaturized Timepix Detector

Matthias Würl, Katrin Schnürle, Jonathan Bortfeldt, Cristina Oancea, Carlos Granja, Enrico Verroi, Francesco Tommasino and Katia Parodi

Cite as:
M. Würl *et al*., "Proton Radiography for a Small-Animal Irradiation Platform Based on a Miniaturized Timepix Detector," *2020 IEEE Nuclear Science Symposium and Medical Imaging Conference (NSS/MIC)*, 2020, pp. 1-6, doi: 10.1109/NSS/MIC42677.2020.9508073

DOI:
10.1109/NSS/MIC42677.2020.9508073

Proton Radiography for a Small-Animal Irradiation Platform Based on a Miniaturized Timepix Detector

Matthias Würl, Katrin Schnürle, Jonathan Bortfeldt, Cristina Oancea, Carlos Granja, Enrico Verroi, Francesco Tommasino, and Katia Parodi *Member, IEEE*

***Abstract*—Pre-treatment proton radiography and computed tomography can improve precision of proton therapy. A compact imaging setup for small-animal proton radiography, based on a miniaturized Timepix detector is presented along with results from proof-of-concept experiments. The MiniPIX detector was placed behind a μ-CT calibration phantom with 10 different tissue-equivalent inserts. The intensity of the 70 MeV proton beam was adjusted such that pixel signal clusters from individual protons on the detector could be resolved. Analysis and event filtering on various cluster properties were used to suppress unwanted events. The energy deposition of the selected clusters was converted to water-equivalent thickness (WET) of the traversed material using a conversion curve based on Monte Carlo simulations and measured clusters of protons after traversing PMMA slabs of known thickness. Despite a systematic underestimation of up to 3%, retrieved WET values are in good agreement with ground truth values from literature. The achieved spatial resolution ranges from 0.3 to 0.7 mm for phantom-detector-distances of 1 to 5 cm. Applicability to living animals is currently limited by the relatively long acquisition time of up to 20 minutes per radiography. This obstacle can however be overcome with the latest detector generation Timepix3, allowing to handle higher particle rates and thus requiring shorter irradiation times.**

***Index Terms*—proton radiography, proton radiotherapy, small animal irradiation, particle tracking, Timepix**

I. Introduction

PRECISION of pre-clinical proton irradiation can benefit from image guidance and using beam properties adapted to small animal size. The SIRMIO (Small Animal Proton Irradiator for Research in Molecular Image-guided Radiation-Oncology) project [1] aims at developing a portable solution that can be temporarily or permanently installed at experimental beamlines of existing clinical proton therapy facilities. The clinical beam properties, namely spot size and energy, will be adapted to match requirements of small animal irradiation by using a dedicated energy degradation and focussing system [2]. Complemented by ultra-sound imaging for tumor localization and positron emission tomography or ionoacoustic measurements for proton range verification, pre-treatment proton imaging will play a crucial role to enable precise irradiation.

Despite the generally lower spatial resolution compared to X-ray imaging, the use of protons for imaging in pre-clinical proton irradiation can have several advantages. As proton imaging is foreseen imminently prior to irradiation with the biological specimen already set up in treatment position, errors in positioning can be eliminated without the need for an additional X-ray tube or optical alignment systems. Secondly, volumetric proton imaging, i.e. proton computed tomography (pCT), allows to directly assess the relative (to water) stopping power (RSP) for protons in tissue, which can reduce treatment planning uncertainties in proton therapy [3], [4].

Most (human-scale) pCT systems rely on dedicated detector prototypes for particle tracking and residual range or energy measurement of individual protons [5]. For our pre-clinical irradiation platform, we are developing a single-particle tracking pCT system composed of low material budget floating strip Micromegas detectors for proton tracking and a segmented time projection chamber with vertical Mylar absorbers as residual range telescope [6]. However, at synchrocyclotron-based proton therapy facilities, the high instantaneous particle fluxes would exceed the detection capabilities of this and other contemporary single particle tracking systems. In order to maintain compatibility of our pre-clinical irradiation platform with such facilities, we are therefore in parallel developing a compact setup based on the hybrid pixel detector Timepix. In this work, we present the results of proof-of-concept proton imaging experiments in the context of small animal irradiation, using a miniaturized, Timepix-based radiation camera [7].

II. Materials and Methods

A. Experimental Setup

The proof-of-concept experiments were performed at the physics beamline in the experimental room of the Trento Proton Therapy facility [8] with a proton beam energy of $70.2\,\mathrm{MeV}$. The experimental setup for proton radiography is shown in Fig. 1 and the individual components and settings are described in the following.

A miniaturized radiation camera MiniPIX-Timepix *(ADVACAM s.r.o, Prague, Czech Republic)* [7] was used to detect the position of individual protons [9] after traversing the imaged object, along with their energy deposition in the $300\,\mu\mathrm{m}$ thick silicon sensor chip. The device is based on the hybrid

Manuscript received December 20, 2020. The authors acknowledge financial support from the European Research Council (grant agreement number 725539).

M. Würl, K. Schnürle, J. Bortfeldt and K. Parodi are with the Department of Medical Physics, Faculty of Physics, Ludwig-Maximilians-Universität München, Garching, Germany (e-mail: matthias.wuerl@physik.uni-muenchen.de; katrin.schnuerle@physik.uni-muenchen.de; jonathan.bortfeldt@physik.uni-muenchen.de; katia.parodi@physik.uni-muenchen.de).

C. Oancea and C. Granja are with ADVACAM s.r.o., Prague, Czech Republic (e-mail: cristina.oancea@advacam.com; carlos.granja@advacam.com).

E. Verroi and F. Tommasino are with the Trento Institute for Fundamental Physics and Applications (TIFPA), National Institute for Nuclear Physics (INFN), Povo, Italy (e-mail: enrico.verroi@tifpa.infn.it; francesco.tommasino@tifpa.infn.it). F. Tommasino is also with the Department of Physics, University of Trento, Povo, Italy.

978-1-7281-7693-2/20/$31.00 ©2020 IEEE

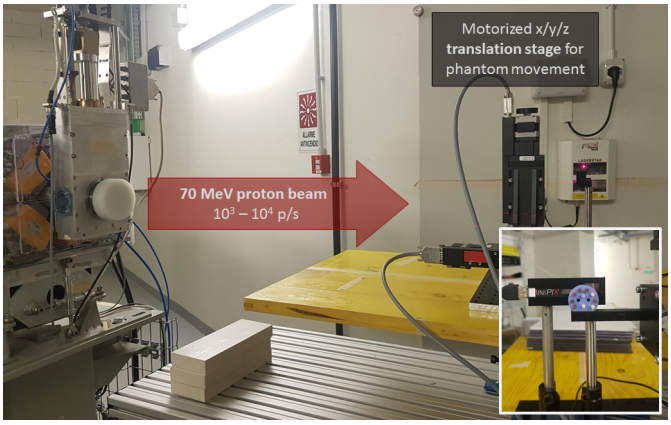

Fig. 1. Experimental setup. The inset shows phantom and detector in beam's eye view.

semiconductor pixel detector Timepix ASIC chip [10], which has a matrix of 256×256 energy sensitive pixels of $55\,\mu\mathrm{m}$ pitch, resulting in a sensitive area of $14 \times 14\,\mathrm{mm}^2$. The high pixel granularity and per-pixel signal electronics can register high event rates with accurate and wide-range spectral and tracking sensitivity. Bias voltage was set to $+30\,\mathrm{V}$ and the frame acquisition time to $40\,\mathrm{ms}$. Considering a frame readout time of $22\,\mathrm{ms}$, this resulted in a frame rate of around 16 frames per second (fps). The detector was operated in per-pixel energy, i.e. Time-over-Threshold (TOT) mode. Pixel values were converted to energy deposition using a previously performed per-pixel TOT-to-energy calibration [11]. Using the in-room laser alignment system, the MiniPIX detector was aligned such that its sensor surface was positioned in the iso-center of the experimental room and the proton beam was normally impinging on the surface.

Due to charge sharing, ionizing particles hitting the sensor generate signal in several adjacent pixels, forming pixel clusters [9]. This allows to determine the position of impinging particles with a sub-pixel resolution by calculating the clusters' center of gravity [9]. Moreover, from the size and shape of the clusters, spectral-tracking information on the particle type and incidence angle can be inferred [7], [12].

In order to keep the number of pile-up events low, i.e. to assure detection of individual and well-separated proton events, the beam intensity in our experiment was reduced to a few 1000 protons per second. This could be achieved by employing the accelerator *dark current* mode available at the beamline of the experimental room [8].

A µ-CT calibration phantom *(SmART Scientific Solutions B.V., Maastricht, Netherlands)*, consisting of a solid water slab ($10\,\mathrm{mm}$ thick, $30\,\mathrm{mm}$ diameter) with 10 cylindrical inserts ($16\,\mathrm{mm}$ length, $3.5\,\mathrm{mm}$ diameter) of tissue-mimicking materials and two air holes was mounted on a 3-axes motorized translation stage. Since the phantom size exceeded the sensor area, the lateral movement with respect to the beam direction allowed to image the entire phantom in 6 steps. The transversal movement was used to increase the air gap between phantom and detector from 1 to $5\,\mathrm{cm}$ in steps of $1\,\mathrm{cm}$ to study the influence of multiple Coulomb scattering (MCS) on the achievable spatial resolution.

In addition to the phantom radiography, open field images were taken, as well as radiographies of homogeneous PMMA plates of 5, 10 and $15\,\mathrm{mm}$ thickness. The proton clusters extracted from these measurements served to identify thresholds for the cluster filtering and to establish a conversion curve for quantitative imaging, as described below.

B. Data Evaluation

Quantitative information on the energy loss of protons in the imaged object was obtained by calculating its water-equivalent thickness (WET). This implied a thorough analysis and filtering of all identified clusters, followed by the conversion from the energy deposition of individual protons in the silicon sensor to the WET of the traversed object. For the latter, a Monte Carlo (MC) model of the experimental setup was created.

1) Cluster Analysis and Filtering: In a first step, the following properties were determined for each cluster and used afterwards to filter out *bad* events, which may originate from pile-up, secondary particles, large-angle incident protons or incomplete charge collection:

- Position x, y, determined by the cluster's center of gravity
- Size s (the number of pixels forming the cluster)
- Length l (the particle track length across the detector semiconductor sensor)
- Eccentricity ϵ of the cluster
- Total energy deposition E_{dep} (the sum of all pixel energy values of the cluster)
- Height h (the highest per-pixel energy deposition in the cluster)
- Maximum position x_h, y_h (the position of the pixel with the highest per-pixel energy deposition)

Based on the analysis of clusters acquired both in an open field configuration and with a $15\,\mathrm{mm}$ PMMA plate, thresholds for cluster acceptance and rejection were established. Clusters with s, l, E_{dep}, ϵ, h/E_{dep} and a distance $\sqrt{(x-x_h)^2+(y-y_h)^2}$ outside these determined thresholds were excluded for further processing. Note that the choice of these thresholds strongly depends on the thickness and material of the sensor chip, the detector settings (e.g. bias voltage) and the expected kinetic energy of the protons reaching the sensor. Moreover, an additional cut for cluster acceptance was introduced to reject outliers in terms of E_{dep}. To this aim, for each pixel the median of E_{dep} of all clusters within that pixel and the surrounding pixels was calculated. Only clusters within 20% and 80% of that value were accepted.

For the remaining clusters, straight and parallel proton paths through the object were assumed and they were spatially re-binned into $0.1 \times 0.1\,\mathrm{mm}^2$ image pixels. As the final radiography of the entire phantom is composed of 6 sub-radiographies of the phantom with respect to the detector, the cluster position (x, y) was corrected for the position of the motorized translation stages.

2) Monte Carlo Model of the Experimental Setup: A FLUKA (version 2020.0.3) [13], [14] MC model of the experimental setup was created, including a simplified model of the MiniPIX detector. The proton source was modelled according

to available information on the beam properties [2], [8]. A $14 \times 14 \times 0.8\,\mathrm{mm}^3$ silicon cuboid, mimicking the sensor and readout chip, was placed with its front surface at a distance of $125\,\mathrm{cm}$ from the proton source. The upstream $0.3\,\mathrm{mm}$ thickness of the cuboid was considered to be the sensor chip, in which energy deposition was scored on an event-by-event basis on a scoring grid of $2816 \times 2816 \times 3$ voxels. Similar to [15], each detector pixel was hence subdivided into $11 \times 11 \times 3$ sub-volumes of size $5 \times 5 \times 100\,\mu\mathrm{m}^3$.

In a post-processing routine, an empirical approach was chosen to model charge sharing and the respective cluster formation from the voxelised per-event energy deposition. For each of the three $100\,\mu\mathrm{m}$ thin layers, the 2-D energy deposition was smeared by a weighted sum of two 2-D Gaussian functions with one narrow and one broad component, respectively. The variance of both components was largest in the first layer and decreased for the central and last layer. Finally, all sub-volumes belonging to one pixel were summed up and pixels with a total energy deposition below $5\,\mathrm{keV}$ were set to zero to account for the energy threshold in the detector settings. The thus generated cluster list was saved in the same format as the output of the experiment and was analyzed using the methods described in II-B1. Since the not only cluster size and shape, but also the total energy deposition within the cluster depends on the choice of variances and weigths used for the Gaussian smearing of the energy deposition, they were varied in a trial-and-error process until the distribution of cluster parameters (s, h, E_{dep}) from simulations matched experiments from open-field images and radiographies of PMMA plates.

3) Water-equivalent Thickness Calculation: From the acquired open-field images and images of the PMMA plates, an inhomogeneity of the detector response in terms of energy deposition was noted. This might be either related to an inhomogeneous depletion of the sensor chip for the used bias voltage and the corresponding loss of ionization charge created by the protons, or due to radiation damage that was accumulated in the time between the TOT-to-energy calibration and our experiments. However, since with and without PMMA plates no spatial dependence of the deposited energy in the sensor chip would be expected, the deviation from the mean was used to equalize the response. That means, depending on the pixel position, the total energy deposition of all clusters in that pixel was corrected via a linear equalization function. As an example, the observed mean energy deposition map after $15\,\mathrm{mm}$ PMMA, before and after equalization is shown in Fig. 2.

For each image pixel, the median corrected E_{dep} was then calculated from all clusters remaining after filtering. To convert this value to WET of the traversed material, a FLUKA MC based conversion curve was created. This required a set of simulations with a water column of varying thickness ($0.5\,\mathrm{mm}$ to $35\,\mathrm{mm}$ in steps of $0.5\,\mathrm{mm}$) placed in front of the Timepix detector. The clusters obtained from these simulations were analyzed and filtered as described in II-B1. The median E_{dep} for each water thickness was then extracted and used to set up the conversion curve, shown in Fig. 3.

This conversion curve then served to translate the median energy deposition to WET. Finally, the determined WET distribution was median-filtered to reduce image noise.

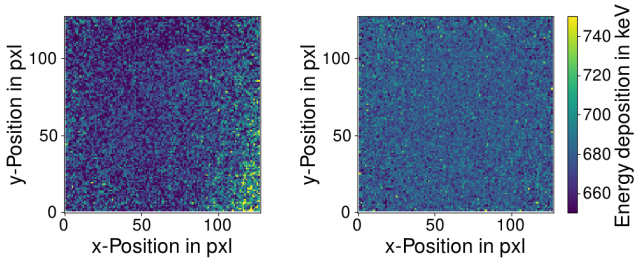

(a) Before equalization (b) After equalization

Fig. 2. Measured mean energy deposition after $15\,\mathrm{mm}$ PMMA, (a) before and (b) after equalization.

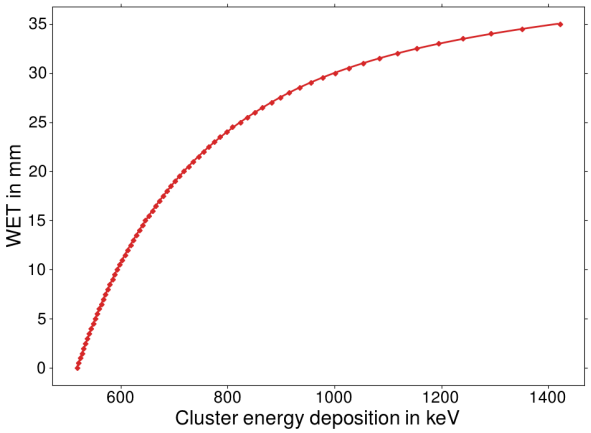

Fig. 3. Conversion curve relating median energy deposition to traversed WET.

III. Results

A. Water-equivalent Thickness Accuracy

The median-filtered WET distribution, determined from the acquired radiographies, is shown in Fig. 4a for a $1\,\mathrm{cm}$ air gap between phantom and detector. In addition, Fig. 4b shows a line profile through the lower part of the phantom, including two bone and one liver substitute inserts. The profile is compared to the ground truth WET profile, which was calculated by multiplying the respective experimentally determined RSP values from [16] with the geometrical object thickness.

A quantitative analysis was done by comparing the mean WET for all 10 inserts with the ground truth. Margins of $0.6\,\mathrm{mm}$ to the insert interfaces were used to define regions-of-interest (ROIs) over which the mean WET and its standard deviation were computed (indicated by the dashed red lines in Fig. 4a). This margin of the ROIs was chosen to allow a disentanglement of the WET accuracy and precision from the spatial resolution. For comparison with the ground truth RSP values from [16], the mean WET for each ROI was divided by the geometrical insert length l_{Ins}. The results are summarized in table I, along with the relative difference with respect to the ground truth. The determined mean WET values are in reasonable agreement with the ground truth values, despite a

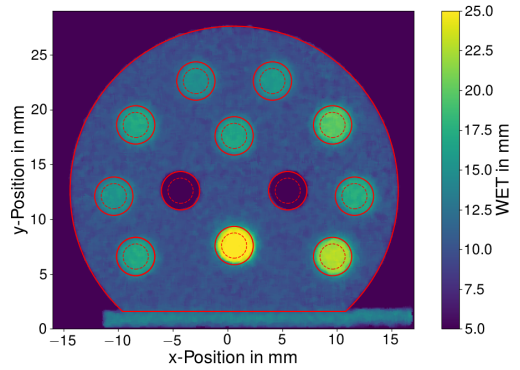

(a) 2-D WET distribution

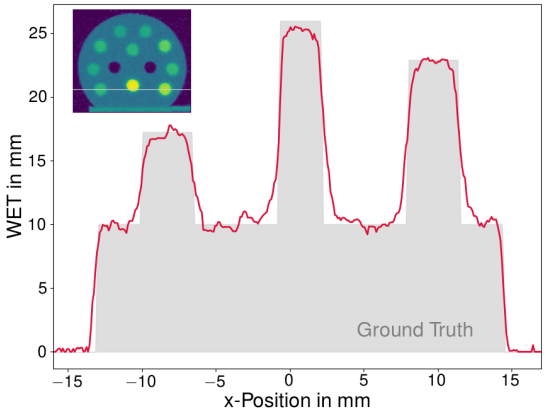

(b) Line profile

Fig. 4. Median-filtered WET distribution (a) and line profile (b). In (a), solid red lines indicate phantom and insert positions, ROIs are shown by dashed red lines. The insert materials, starting from the lower left insert (clockwise) are: liver, breast, inner bone, adipose, solid water, CB2-30% cort. bone, bone (B200), CB2-50% cort. bone; the upper and lower central insert materials are brain and cort. bone (SB3), respectively. In (b), the ground truth WET (according to [16]) is indicated by the grey area, the reconstructed WET is shown in red. The white line in the inset marks the line profile position.

systematic slight underestimation of up to 3% for all materials. The standard deviation of the WET within each ROI, divided by its mean was up to 2.5%, indicating good precision for the total number of protons chosen in our experiment.

TABLE I
COMPARISON OF DETERMINED WET DIVIDED BY THE GEOMETRICAL INSERT LENGTH TO GROUND TRUTH RSP. THE STANDARD DEVIATION IS GIVEN IN BRACKETS.

Insert material	**Ground truth RSP [16]**	**WET / l_{Ins} (std. dev.)**	**Relative difference**
Adipose	0.943	0.927 (0.018)	−1.70%
Breast	0.973	0.962 (0.024)	−1.13%
Solid Water	1.000	0.983 (0.022)	−1.70%
Brain	1.064	1.045 (0.019)	−1.79%
Liver	1.079	1.062 (0.021)	−1.58%
Inner Bone	1.092	1.060 (0.023)	−2.93%
B200 Bone	1.100	1.086 (0.023)	−1.27%
CB2-30% Cort. Bone	1.279	1.245 (0.022)	−2.66%
CB2-50% Cort. Bone	1.434	1.417 (0.020)	−1.19%
SB3 Cort. Bone	1.623	1.586 (0.018)	−2.28%

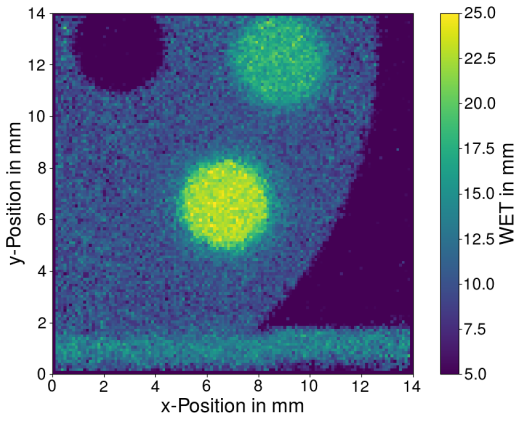

(a) 1 cm air gap

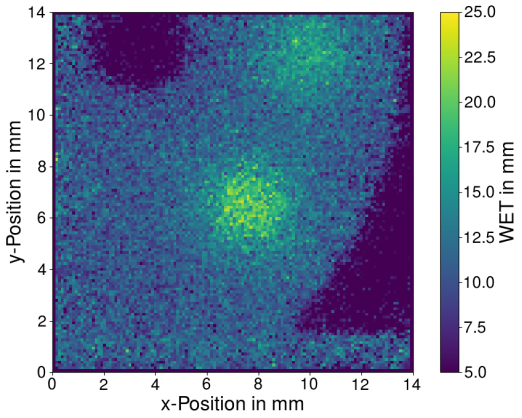

(b) 5 cm air gap

Fig. 5. WET distribution of the lower right part of the phantom for an air gap of (a) 1 cm and (b) 5 cm with the CB2-50% cortical bone insert used for determination of the spatial resolution in the center of the images.

B. Spatial Resolution

The spatial resolution was determined from the edge-spread function at the interface between CB2-50% cortical bone insert and the solid water base plate. The WET distribution of the lower right part of the phantom is shown in Fig. 5a and 5b for air gaps of 1 cm and 5 cm, respectively. The corresponding insert is located in the center of the images.

For the smallest air gap, the spatial resolution was found to be 0.3 mm. An increase of the air gap, i.e. the distance between phantom and detector, gradually leads to more blurring and subsequently lower spatial resolution due to MCS in the phantom. Yet, even with an air gap of 5 cm, the spatial resolution was below 0.7 mm.

C. Imaging Dose and Acquisition Time

As previously pointed out, the frame-based detector readout necessitated such a low beam intensity to limit the number of event pile-up. In order to obtain a sufficiently high number of single proton clusters per reconstructed image pixel, the acquisition time per phantom position was ranging between 15 to 20 min.

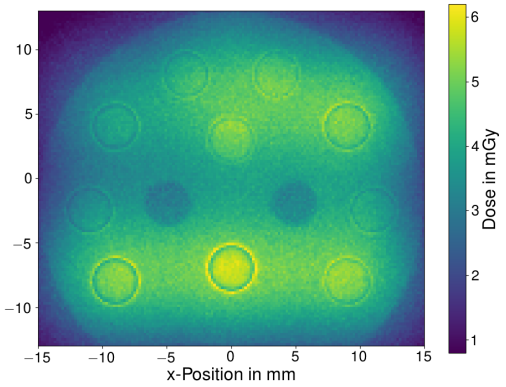

Fig. 6. Imaging dose distribution in the phantom according to FLUKA MC simulations.

Since the imaging dose was not directly measured during image acquisition, it was estimated in subsidiary MC simulations. To this aim, the FLUKA model of the experimental setup (section II-B2) was used to mimic the phantom radiography *in-silico*. The number of primaries in the simulation was adjusted, such that the number of protons reaching the detector in the simulation agreed with the number of measured clusters within 1%. The corresponding imaging dose distribution inside the phantom is shown in Fig. 6. The most prominent dose inhomogeneities are found at the insert interfaces and can be explained by the difference in geometrical length and scattering power of the insert materials compared to the base plate. Further, the rather smooth dose variation over the entire image is firstly due to the Gaussian-like shape of the beam spot and secondly due to small variations in the acquisition time and hence proton count for the radiographies of the indidual phantom positions. All in all, the median of the imaging dose was found to be around $5\,\mathrm{mGy}$.

IV. Discussion

A. Image Quality and Dose

Promising image quality in terms of WET accuracy and spatial resolution were obtained for an estimated imaging dose of $5\,\mathrm{mGy}$. The small systematic WET underestimation of up to 3% may either be related to a minor detector calibration error and the related equalization procedure, or to inaccuracies in the MC-based conversion curve. Both potential sources could be overcome with a re-calibration of the detector and further measurements of clusters after traversing e.g. PMMA slabs of other thicknesses than used in our measurements. Especially larger thicknesses would be of interest, since the WET of most inserts of our phantom is larger than the largest calibration WET of $15\,\mathrm{mm}$ PMMA.

Spatial resolution in proton imaging is limited by MCS inside the imaged object. Although our assumption of straight and parallel proton paths through the object does not account for scattering at all, the obtained sub-mm spatial resolution might still be acceptable for our purpose, given the very small foreseen distances between the object and the detector. In our planned configuration, an air gap of $5\,\mathrm{cm}$ would already be larger than the extreme object-detector distance. To further improve the spatial resolution, a better estimation of the proton path through the object would be essential. This, however, would require an additional tracking detector upstream of the imaged object and would hence increase the system complexity.

Due to the small pixel dimension, imaging doses in conventional small animal X-ray CT scanners are around or even higher than $300\,\mathrm{mGy}$ for a full tomography [17]. Our estimated dose for a single radiography may therefore be a bit elevated, but still acceptable if one considers a full pCT consisting of 90 projections.

A considerable dose reduction while keeping the same image quality and pixel dimensions is hardly possible. Since the WET determination relies on an energy loss measurement of individual protons in a relatively thin detector instead of measuring of their residual energy, fluctuations are much more pronounced. Therefore, the minimum number of events required per pixel will always exceed the number of required protons in systems where residual energy is measured in range telescopes or calorimeters.

B. Strengths and Limitations of the Current Setup

A major advantage of the proposed setup is its very compact size and simple operation as compared to e.g. tracker- and range-telescope based solutions. The miniaturized Timepix detector is commercially available and comes with a user-friendly acquisition software. With a TOT-to-energy calibration and after establishing a relatively straight-forward WET calibration as described in section II-B3, absolute and spatially resolved WET measurements with reasonable accuracy and resolution are possible with this portable and stand-alone detection system.

On the other hand, the acquisition time of the presented setup is long, and it would be prohibitively long for imaging of living samples, especially when aiming for pCT imaging. The MiniPIX detector used in this study is based on the Timepix ASIC which only supports frame-based readout with a maximum frame rate of $45\,\mathrm{fps}$. In our study, a much lower frame rate was chosen. This was motivated by the frame readout time of $22\,\mathrm{ms}$, during which no charge is collected from the sensor. With a continuous proton irradiation, i.e. the beam is on during detector dead time, exploiting the full frame rate would have therefore resulted in a considerably higher imaging dose.

This limitation, however, is not a conceptual problem of the setup but is attributed to the detector available during our experimental campaign. The successor model of the miniaturized Timepix detector is based on the Timepix3 ASIC [18]. Apart from an improved energy resolution, this detector also supports event-based readout and has therefore practically no dead time. With the increased data rates, imaging at a considerably higher beam intensity would be feasible before problems of proton pile-up or limitations of the data rate would be encountered. Assuming an average cluster size of 10 to 12 pixels and taking into account the maximum rate of 2.3×10^6 hit pixels per second, as specified by the manufacturer, a

reduction of imaging times per radiography below $20\,\mathrm{s}$ would be possible. Further reduction of imaging time can be achieved by Timepix3-based fast readout electronics supporting higher data rates, however at the cost of a less compact setup.

Another issue contributing to the long imaging time is the relatively small sensor area, which is smaller than the typical imaging field-of-view for small-animal studies. In our proof-of-concept study, this shortcoming was dealt with by several lateral movements of the object with respect to the fixed beam and detector and by creating a stacked image of all sub-radiographies. However, using existing large-area arrays of e.g. 2×1 Timepix chips and a sufficiently broad beam already reduces the number of required lateral movements and hence the total imaging time by a factor of 2.

Since the motivation of this study is the development of an imaging setup compatible with synchrocyclotron-based proton therapy facilities, the preceding discussion can also be extend to this aspect. For the MiniPIX detector used in our experiments, it is irrelevant whether the protons hitting the detector within each frame are bunched in few µs short pulses or whether they arrive continuously, as long as the number of protons per frame is still low enough to avoid pile-ups. For the successor model, the considerations can be done in a similar manner. Since the per-pixel signal shaping time is well below the time between proton pulses of clinical synchrocyclotrons ($\approx 1\,\mathrm{ms}$), the interaction of protons from one pulse with the detector has no impact on the interaction of protons from following pulses. Therefore, as long as the number of protons per pulse is low enough to avoid pile-ups, the preceding discussions on imaging time are also valid for proton imaging at synchrocyclotron-based facilities.

V. Conclusion

A proof-of-concept experiment for pre-clinical proton imaging, based on a high-granularity miniaturized Timepix detector was presented. While imaging time in the current setup appears too long for imaging of living animals, WET accuracy and spatial resolution are promising and encountered systematic WET errors might be corrigible. Replacing the detector used in this study by its already available successor Timepix3 will considerably reduce acquisition time and may hence provide a compact and user-friendly solution for small animal proton imaging.

Acknowledgment

The authors would like to thank A. Empl for the fruitful discussion on the FLUKA simulation model of the detector.

References

[1] K. Parodi, W. Assmann, C. Belka, J. Bortfeldt, D.-A. Clevert, G. Dedes, et al., "Towards a novel small animal proton irradiation platform: the SIRMIO project," Acta Oncologica, 58, 1470–1475, 2019.

[2] S. Gerlach, M. Pinto, N. Kurichiyanil, C. Grau, J. Herault, M. Hillbrand, et al., "Beam characterization and feasibility study for a small animal irradiation platform at clinical proton therapy facilities," Physics in Medicine and Biology, 2020 (accepted for publication).

[3] N. Arbor, D. Dauvergne, G. Dedes, J.M. Létang, K. Parodi, C.T. Quiñones, et al., "Monte Carlo comparison of x-ray and proton CT for range calculations of proton therapy beams," Physics in Medicine and Biology, 60, 7585, 2015.

[4] G. Dedes, J. Dickmann, K. Niepel, P. Wesp, R.P. Johnson, M. Pankuch, et al., "Experimental comparison of proton CT and dual energy x-ray CT for relative stopping power estimation in proton therapy," Physics in Medicine and Biology, 64, 165002, 2019.

[5] R. P. Johnson, "Review of medical radiography and tomography with proton beams," Reports on Progress in Physics, 81, 1, 2017.

[6] S. Meyer, J. Bortfeldt, P. Lämmer, F. S. Englbrecht, M. Pinto, K. Schnürle, et al., "Optimiyation and performance study of a proton CT system for pre-clinical small animal imaging," Physics in Medicine and Biology, 65, 155008, 2020.

[7] C. Granja, K. Kudela, J. Jakubek, P. Krist, D. Chvatil, J. Stursa, and S. Polansky, "Directional detection of charged particles and cosmic rays with the miniaturized radiation camera MiniPix Timepix," Nuclear Instruments and Methods in Physics Research Section A, 911, 142–152, 2018.

[8] F. Tommasino, M. Rovituso, S. Fabiano, S. Piffer, C. Manea, S. Lorentini, et al., "Proton beam characterization in the experimental room of the Trento Proton Therapy facility," Nuclear Instruments and Methods in Physics Research Section A, 869, 15–20, 20, 2017.

[9] J. Jakubek, A. Cejnarova, T. Holy, S. Pospisil, J. Uher, and Z. Vykydal, "Pixel detectors for imaging with heavy charged particles," Nuclear Instruments and Methods in Physics Research Section A, 591, 155–158, 2008.

[10] X. Llopart, R. Ballabriga, M. Campbell, L. Tlustos, and W. Wong, "Timepix, a 65k programmable pixel readout chip for arrival time, energy and/or photon counting measurements," Nuclear Instruments and Methods in Physics Research Section A, 581, 1-2, 2017.

[11] J. Jakubek, "Precise energy calibration of pixel detector working in time-over-threshold mode," Nuclear Instruments and Methods in Physics Research A, 633, pp S262–S266, 2011.

[12] C. Granja, J. Jakubek, S. Polansky, V. Zach, P. Krist, D. Chvatil, et al., "Resolving power of pixel detector Timepix for wide-range electron, proton and ion detection," Nuclear Instruments and Methods in Physics Research A, 908, 60–71, 2018.

[13] T.T. Böhlen, F. Cerutti, M.P.W. Chin, A. Fassó, A. Ferrari, P.G. Ortega, et al., "The FLUKA Code: Developments and Challenges for High Energy and Medical Applications," Nuclear Data Sheets 120, 211–214, 2014.

[14] A. Ferrari, P.R. Sala, A. Fassó, and J. Ranft, "FLUKA: a multi-particle transport code," CERN-2005-10, INFNTC_0511, SLAC-R-773, 2005.

[15] M. Kroupa, T. Campbell-Ricketts, A. Bahadori, and A. Empl, "Techniques for precise energy calibration of particle pixel detectors," Review of Scientific Instruments, 88, 033301, 2017.

[16] N. Hudobivnik, F. Schwarz, T. Johnson, L. Agolli, G. Dedes, T. Tessonnier, et al., "Comparison of proton therapy treatment planning for head tumors with a pencil beam algorithm on dual and single energy CT images," Medical Physics, 43, 495, 2016.

[17] F. Verhaegen, L. Dubois, S. Gianolini, M.A. Hill, C.P. Karger, K. Lauber, et al., "ESTRO ACROP: Technology for precision small animal radiotherapy research: Optimal use and challenges," Radiotherapy and Oncology, 126, 3, 2018.

[18] T. Poikela, J. Plosila, T. Westerlund, M. Campbell, M. De Gaspari, X. Llopart, et al., "Timepix3: a 65K channel hybrid pixel readout chip with simultaneous ToA/ToT and sparse readout," Journal of Instrumentation, 9, C05013, 2014.